 doi:10.20944/preprints202104.0311.v1

Chitosan/Silver Nanoparticle/Graphene Oxide Nanocomposites with Multi-drug Release, Antimicrobial, and Photothermal Conversion Functions

Zheng Su[a,b], Daye Sun[b], Li Zhang[c], Miaomiao He[c], Yulin Jiang[c], Bronagh Millar [b], Paula Douglas [b], Davide Mariotti[d], Paul Maguire[d], Dan Sun[*,b]

a. Department of orthopedics, The First Affiliated Hospital of USTC, Division of Life Sciences and Medicine, University of Science and Technology of China, Hefei, Anhui 230001, China
b. School of Mechanical & Aerospace Engineering, Queens University Belfast, Belfast, BT9 5AH, UK
c. Research Center for Nano-Biomaterials, Analytical & Testing Center, Sichuan University, Chengdu 610065, China
d. Nanotechnology and Integrated Bioengineering Center (NIBEC), Ulster University, Co Antrim BT37 OQB, UK
Correspondence: d.sun@qub.ac.uk; Tel.: +44 (0) 28 90974701

Abstract: In this work, we designed and fabricated a multifunctional nanocomposite system which consists of chitosan, raspberry-like silver nanoparticles and graphene oxide. Room temperature atmospheric pressure microplasma (RT-APM) process provides a rapid, facile, and environment-friendly method for introducing silver nanoparticles into the composite system. By loading different drugs onto the polymer matrix and/or graphene oxide, our composite can achieve a pH controlled dual drug release with release profile specific to the drugs used. In addition to its strong antibacterial ability against E. coli and S. aureus, our composite also demonstrates excellent photothermal conversion effect under irradiation of near infrared lasers. These unique functionalities point to it's the potential of nanocomposite system in multiple applications areas such as multimodal therapeutics in healthcare, water treatment, and anti-microbial, etc.

Keywords: Chitosan; Silver nanoparticles; Graphene oxide; Nanocomposites; Antibacterial property; Drug delivery

1. Introduction

Chitosan (CS) exhibits biocompatibility and biodegradability and has been explored widely for biomedical applications such as bone/skin regeneration, wound dressing and cancer therapy [1-3]. Graphene oxide (GO), on the other hand, has excellent mechanical properties and electrical conductivity [4]. Its high specific surface area and oxygen-containing surface functional groups has enabled its application as drug carrier [5, 6]. In addition, GO has also emerged as promising photothermal agents for photothermal therapy especially due to their high absorption cross-sections in the near infrared (NIR) region [7, 8]. These unique physio-chemical properties have enabled its wide applications in the biomedical field, including drug delivery, photothermal therapy and tissue regeneration [9, 10].

Combining CS with GO could lead to nanocomposites with unique functionality for wider range of applications, particularly in the biomedical field. For instance, Barra et al.[11], developed electrically conductive chitosan - reduced graphene oxide flexible bionanocomposites for food packaging and biological applications. Hermenean et al.[12], fabricated chitosan-graphene oxide 3D scaffold via pi-pi interaction, where the resulting composites has been proposed for bone regeneration. Rana et al.[13], used CS to surface functionalize GO through chemical crosslinking, the in-vitro study showed the higher cell viability of the functionalized GO. Bao et al.[14], fabricated biocompatible CS-functionalized GO, which can be used as nano-carrier for drug and gene delivery. Shamekhi et al.[15], prepared GO containing CS scaffolds for cartilage tissue engineering with enhanced physical and mechanical properties via cross-linking and incorporation of nanoparticles. Liu et al.[16], obtained the three-dimensional (3D) CS/GO scaffolds with aligned

 doi:10.20944/preprints202104.0311.v1

pores for tissue engineering with enhanced mechanical strength, shape-memory, cell alignment guiding capabilities, and protein adsorption ability. The GO was also used to improve the electrical conductivity of biomaterials in cardiac tissue engineering [17, 18].

In recent years, there is an increasing demand for multi-functional materials, particularly in the biomedical field. For instance, enabling simultaneous anti-microbial and drug release functions is of particular interest for conditions such as osteogenesis, inflammation, and infections [19, 20]. Effective anti-bacterial and drug delivery functions combined with photothermal therapy may enable multimodal therapeutic functions with enhanced treatment efficacy towards challenging health conditions such as cancer [21, 22] and severe arthritis [23].

Room temperature atmospheric pressure microplasma (RT-APM) process is a rapid, facile, and environment-friendly method that can be used to prepare nanocomposites. The resulting nanocomposites consisting of CS with embedded silver nanoparticles through RT-APM have demonstrated tailored structure/properties as well as promising antibacterial activity against E. coli and S. aureus [24]. One interesting aspect worth further investigation is the addition of other functional nanomaterials (e.g., photothermal conversion agents) into this system to form a hybrid multi-functional nanocomposite and to further demonstrate the potential of such hybrid nanocomposites for a wider range of biomedical applications.

In this work, GO was introduced into the RT-APM synthesized CS/raspberry-like silver nanoparticles (RB-AgNPs) system to produce a CS/RB-AgNPs/GO hybrid nanocomposite. The resulting hybrid composites were then characterized for their structure and properties via SEM, TEM, UV-vis, FT-IR, and TGA, DSC, and their functionality towards anti-microbial, drug release and photothermal conversion has also been demonstrated.

2. Materials and Methods

2.1 Materials

Chitosan (CS, low molecular weight 50,000-190,000 Da, 75-85% deacetylated), silver nitrate (AgNO3, ACS reagent, ≥99.0%), fluorescein sodium, methylene blue, and phosphate buffered saline (PBS) tablets (pH=7.4) were purchased from Sigma-Aldrich (United Kingdom). Graphene oxide (5 mg/mL aqueous solution, flake size: 0.5-5 μm, 1 atomic layer at least 60%) was purchased from Graphene Laboratories, Inc. Acetic acid (puriss, glacial, ≥99.9%) was obtained from Riedel-de Haën Sigma-Aldrich Laborchemikalien GmbH. Ultrapure water (>18.2 MΩ cm Millipore Milli-Q system) was used in the all experiments. Helium gas was purchased from BOC, UK. Methylene blue (MB) and fluorescein (FL) were obtained from Sigma-Aldrich, UK.

2.2 Fabrication CS/RB-AgNPs/GO nanocomposite

Room temperature atmospheric pressure microplasma (RT-APM) process as a rapid, facile, and environment-friendly method was used to synthesize CS/RB-AgNPs. More specifically, as purchased CS powder was dissolved in 2% (v/v) acetic acid and stirred for 24 hours under room temperature to obtain a 2% (w/v) homogeneous solution. Appropriate amount of AgNO3 (50mN) was added to the CS solution to obtain precursor solution CS+AgNO3 mixture. The mixture was subject to RT-APM treatment see in Scheme 1 (a), gives the details of RT-APM setup. A stainless steel capillary cathode (0.25 mm inner diameter and 0.5 mm outer diameter) was placed ~ 1.5 mm above the solution surface, and a carbon rod (anode) was immersed in the liquid. Helium gas was passed through the cathode capillary at a flow rate of 25 SCCM, a constant current of 5 mA and voltage of 0.7-1.0 kV was maintained during the plasma treatment. The RT-APM treatment was carried out for 10 min and the samples were stirred during the treatment to obtain a well-mixed colloid (see Scheme 1 (b)). The resulting sample is named as CS/RB-AgNPs.

The CS/RB-AgNPs/GO nanocomposite with 0, 0.5, and 1.5 wt% GO were prepared by adding appropriate amount of GO into the RT-APM treated CS/RB-AgNPs sample. All liquid samples were then transferred into a Teflon mould (with 9 mm diameter × 4 mm

 doi:10.20944/preprints202104.0311.v1

recess) and the samples were frozen over night at -35 °C, followed by freeze-drying (Lyotrap LTE) for 24 hours at -60 °C. Table 1 shows the composition and nomenclatures of the samples prepared in this study.

2.3 Characterization

Fourier transform infrared spectrometer (FTIR, Perkin Elmer Spectrum 100 ATR, 4 cm-1 resolution and 36 scans per sample) was used to analyse the samples. Thermogravimetric analysis (TGA, TA Instruments SDT-Q600) was carried out under nitrogen atmosphere over the temperature range 40 - 600 °C at 10 °C per min increment. The morphology of the cryo-fractured sample (gold sputtered) was observed by scanning electron microscopy (SEM, HITACHI FlexSEM 1000) with acceleration voltage in the range of 5-15 kV. Differential Scanning Calorimeter (DSC) was carried out using Perkin-Elmer DSC 6 instrument. The samples were first scanned from 20~110°C at 10°C/min to remove water and eliminate thermal stress, The samples were then held at 110°C for 10 min and cooled from 110°C to 20°C at 10°C /min. The second scan was carried out from 20°C to 380°C at 10°C/min. UV-vis spectroscopy (Cary Win UV) was used to characterize drug release under pH 7.4 and pH 4, respectively. X-Ray Diffraction (XRD, PANalytical X'PERT ProMPD) was used to analyse the crystallinity of samples. Lloyd's LRX Tensile Tester was used for the Quasi-static mechanical testing in compression with 50 N load cell, following ASTM D1621-101 with specimen sizes (10 mm diameter, 5 mm height).

2.4 Drug releasing tests

Two model drugs FL and MB have been selected. To investigate the single drug release profile, FL loaded GO (1.5 mg FL per 100 mg GO), namely (GO-1.5)-FL or MB loaded CS/RB-AgNPs (0.2 mg MB per mL of CS/RB-AgNP colloid)), namely (CS/RB-AgNPs)-MB, was used to prepare the single drug laden nanocomposite, respectively. For dual drug release, both FL loaded GO and MB loaded CS/RB-AgNPs were used. Three types of drug loaded nanocomposites were prepared, namely, (CS/RB-AgNPs)-MB/GO-1.5, CS/RB-AgNPs/(GO-1.5)-FL, and (CS/RB-AgNPs)-MB/(GO-1.5)-FL. Drug release test was conducted in 10 mL PBS (pH 7.4 or 4.0, 37 °C). At different time intervals, 2.5 mL of test solution was analysed using UV-vis spectrophotometer and the remaining solution was topped up with fresh PBS. The cumulative release percentage of FL and MB was calculated following Equation (1):

$$\text{Cumulative drug release (\%)} = M_t/M_0 \times 100\% \quad (1)$$

Where Mt is the amount of drug released at time t and M0 is the initial amount of drug load.

2.5 Antibacterial tests

The antibacterial properties of the nanocomposites were evaluated by zone of inhibition test using Staphylococcus aureus (Gram-positive bacteria) and E.coli (Gram-negative bacteria) respectively. 100 µl of the overnight bacterial culture (1 × 108 CFU/ml) was spread on Nutrient Agar plates. The sample was then placed in the plates in triplicates followed by incubation for 24 h at 37 °C. After the incubation period the zone of inhibition was measured.

2.6 Photothermal conversion behaviour tests

IR thermal camera (FORTIC 220RD PCBA) is used to capture the thermal image of samples under near infrared (NIR) 808 nm laser irradiation with different powers (0.2, 0.4, 0.6, and 1.0 W) with a light window of 50.24 mm2.

3. Results

3.1 Materials characterization

Fig. 1 (a) shows the UV-vis spectra of all testing samples. In theory, GO should have an absorbance peak at around 200 nm due to the pi -pi* conjugation of C=C bonds [25]. However, this peak overlaps with the characteristic peak of pure CS at 200-250 nm and cannot be easily distinguished in the spectra of the CS/RB-AgNPs/GO composite samples. Optical images in Fig.1 (a) inset shows the change of solution colours for different samples, where brown color is indicative of presence of RB-AgNPs. The presence of RB-AgNP

 doi:10.20944/preprints202104.0311.v1

is further supported by the typical broad surface plasmon resonance (SPR) absorption (~ 410 nm) for RB-AgNPs. The TEM images in Fig. 1 (b) shows the morphology and size distribution of RB-AgNPs in CS/RB-AgNPs/GO-1.5 solution with average size of 73.69 nm.

Fig. 2 (a) presents the photographs of nanocomposites with different RB-AgNP and/or GO contents. The TGA results provide better understanding of the thermal decomposition and thermal stability of pure chitosan and composites. Pure CS has an initial decomposition at 270.16 °C due to the thermal degradation of polymer chains. As shown in Fig. 2 (b), all TGA curves have similar decomposition trend. And the weight loss around 127.32 °C is attributed to the loss of water from the polymer. Interestingly, the loading of RB-AgNPs and GO delay the initial decomposition of the CS's polymer chains, however, has higher residual mass from 40.25 % to 41.83 % at 700 °C than pure CS. The decomposition hindering effect can explain this phenomenon [26].

Fig. 2 (c) shows the DSC curve of pure CS, CS/RB-AgNPs, and CS/RB-AgNPs/GO composites obtained from the second heating. The CS chain segmental mobility could be reflected by the glass transition temperature (Tg). The Tg of pure CS is 134.70 °C and the broad baseline step is due to the rigidity of the CS molecular structure [27]. The addition of RB-AgNPs increased the Tg of CS/RB-AgNPs composites to 138.89 °C, whereas the presence of both GO and RB-AgNPs increased the Tg of CS/RB-AgNPs/GO composites to 141.91 °C. The increase in Tg is ascribed to the interaction between CS chains and GO sheets and RB-AgNPs [28, 29]. Such interaction may constrain the segmental motion of CS chains by hydrogen bonding and electrostatic interaction and hence increase its thermal stability [30]. The exothermic peak around 270-350 °C shown in Fig. 2 (c) and Table S1 both indicate the thermal decomposition of composites, which can be further related to the material weight loss seen in the TGA curves (Fig. 2 (b)).

Fig. 2 (d) presents the FT-IR spectra of all samples. The characteristic bands of amide I and amide II groups are located at 1654 cm-1 and 1385 cm-1. The peaks at 1333 cm-1 and 1258 cm-1 belong to the O-H bending vibration, and the anti-symmetrical stretching of C-O-C bridge can be found at 1151 cm-1 [31, 32]. The strong broad band at 3100-3650 cm-1 represents characteristic peak of N-H or O-H stretching vibration from CS, RB-AgNPs or GO [33]. The intensity of N-H bending vibration peak at 1532 cm-1 decreases due to the interaction between RB-AgNP and CS through hydrogen bonding [31].

3.2 Mechanical properties

Further SEM analysis in Fig. 3 shows that the influence of nanofillers on the composites' microstructure and mechanical property (compressive modulus). Nano-sized RB-AgNPs led to reduced pore size but greater pore density when compared with pure CS. Whereas CS/RB-AgNPs containing GO sheets with flake size of 0.5-5 μm shows more similar structure to pure CS. Fig. 3 (d) shows the mean compressive elastic modulus of composite samples. The increased modulus for CS/RB-AgNPs may can be attributed to hydrogen bond formation between nanofillers and polymeric matrix, resulting in restricted motion of backbone chain [34]. When GO is introduced into the system, RB-AgNPs (or CS encapsulated RB-AgNPs) may interact preferably with the GO flakes through physical adsorption or electrostatic interaction [35]. This may lead to agglomeration of the nanofillers (also see Fig S2), which can deteriorate the composite mechanical property (reduced stiffness).

3.3 In-vitro drug release profiles

FL and MB were selected as type model drugs as their molecular weights are similar to some of the anti-cancer, anti-inflammatory, and bone regeneration drugs (such as Cisplatin, Not-steroidal anti-inflammatory indomethacin, Dexamethasone, FTY20, Vitamin D3, Sphingosine-1, etc.) [36]. The successful loading of FL onto GO (GO-FL) can be confirmed by the UV-vis spectroscopy. Fig. 4 (a) shows the UV-vis spectra of GO, GO-FL, and the as-prepared FL solutions. The original characteristic peaks of FL (238, 459 nm and 491

 doi:10.20944/preprints202104.0311.v1

nm) were blue shifted to231 nm, 448 nm and 483 nm in the GO-FL sample. The characteristic peaks of MB at 292 nm and 663 nm remain unchanged after loaded onto CS/RB-AgNPs. These characteristic peaks were used to investigate the release of MB in solution (Fig. 4 (b)).

For in-vitro drug release tests, we loaded MB onto CS/RB-AgNPs matrix and loaded FL onto GO to form the two separate single drug release models. Subsequently, we combined MB laden CS/RB-AgNPs and FL laden GO to obtain the dual drug release system. Fig. 5 presents the percentage of cumulative drug released in neutral (pH=7.4) and acid (pH=4.0) environment over 240 h. For single drug release of MB (MB on CS/RB-AgNPs) (Fig. 5 (a)), a burst release was evident under pH 7.4 in first 10 h, followed by a more stabilised release of 70-80% after 40-50 h. Under pH 4, however, the release rate was significantly accelerated the drug release reached 100 % from 80 h. In contrast, the single drug FL (FL on GO) (Fig. 5 (b)) release shows a time lag behaviour. Only 30% FL was released in the first 10 h under pH 7.4 and the cumulative release only increased slowly up to 45% towards the end of 240 h. The lower of pH also significantly altered the release profile, which featured a continue increase of cumulative drug release at a much higher rate throughout the measurement period. Fig. 5 (c) and (d) shows the drug release profile of CS/RB-AgNPs/GO-1.5 when it acted a dual release system (MB in CS/RB-AgNPs and FL on GO). It can be seen from Fig. 5 (c) that the addition of FL (FL-GO to replace GO) slowed down the MB release rate for both pH conditions as compared with the single drug (MB) release system. In contrast, when MB-loaded CS/RB-AgNPs was used, the FL release rate from CS/RB-AgNPs/GO-1.5 was only increased slightly under both pH conditions.

3.4 In-vitro drug release kinetic model

In order to obtain a suitable drug release model that best describes the drug release profile, several kinetic models have been considered for the drug release systems involved in this study, these include zero order (cumulative percent drug released versus time), first order (log cumulative percent drug retained versus time), Higuchi (cumulative percent drug released versus√time), and Korsmeyer-Peppas (log cumulative percent drug released versus log time) and the curve fitting results were shown in Table 2, Fig. S3 and Fig. S4 [37]. The modelling accuracy was evaluated by comparing the coefficient of determination (R2) values. In the Korsmeyer-Peppas (Fickian diffusion) model, the mechanism of drug release was indicated by the value of the release exponent N [38, 39]. Porous structures typically exhibit N<0.45 and diffusion occurs through water-filled pores and through polymer layer due to the swollen matrix [40, 41].

The drug release kinetic analysis results from Table S2 suggests that the Korsmeyer-Peppas model best describes the predominant release mechanism for both single and dual drug systems (Fig. 6). The porous structure of the composites were corroborated by the value of release exponent N < 0.45. When fitting the drug release curves based on the Korsemeyer-Peppas model [42], the cumulative amount of drug release (Mt) could be described by equation (2):

$$M\_t=kt^N \quad (2)$$

Where N was the release exponent in Korsmeyer-Peppas model, indicative the drug release mechanism, t was the time elapsed and k was defined by equation (3):

$$k=A\sqrt{(2C\_init\ DC\_s)} \quad (3)$$

Where A was the cross sectional area of the cylinder (diameter=1.0 cm, height=0.5 cm), C_init was original concentration of the drug (MB=0.2 mg/mL and FL=1.5 wt%), C_s was the solubility (70 mg/mL for MB and 500 mg/mL for FL) and D was the diffusion coefficient of the drug (0.42×10-5 cm2/s for pristine FL and 0.79×10-5 cm2/s for pristine MB) [43].

For the dual drug system, the true diffusion coefficient of MB and FL is different from the ideal diffusion coefficient due to the potential host-guest and guest-guest interactions[44] between GO, MB, and FL see Fig. 7 and Table 2.

In our drug laden composites, FL was loaded onto GO via weak pi-pi interaction, which can be described as a weak host (GO)-guest (FL) interaction. When MB was introduced into the system, the stronger ionic interaction between MB and GO (host (GO)-guest (MB)) drove, replacement of the loosely adsorbed FL with MB, to form a more stable structure, leading to a slower MB but greater FL release. In addition, the repulsive force between the negatively charged functional groups on FL and GO accelerate the desorption process of FL from GO sheet surface. The true diffusion coefficients (DK) of each system following Korsemeyer-Peppas model were obtained through further optimization towards the objective function, see Table 2.

3.5 Antibacterial ability

Inhibition zones of the composite samples were measured to evaluate their antibacterial ability against E. coli and S. aureus, see Fig. 8. It can be seen that pure CS exhibits no visible antibacterial ability. In contrast, samples containing RB-AgNPs showed significantly enhanced antibacterial performance. The presence of RB-AgNPs can generate reactive oxygen species (ROS) when in contact with the bacterial strains, and these ROS could destabilize the bacteria plasma membrane potential, deplete the levels of intracellular adenosine triphosphate, and eventually lead to the death of bacterial cells [45]. Increased GO content also leads to further enhanced antibacterial ability, because GO can cause oxidative pressure [46] or bacterial cell membrane damage [47].

3.6 Antibacterial ability

All samples were immersed in PBS solution and their photothermal conversion behaviour under 808 nm laser irradiation have been examined, using PBS solution as the control. Fig 9 (a) and (b) show that under 1W laser irradiation, samples containing no GO exhibited no photothermal conversion effect. For CS/RB-AgNPs/GO composites, the sample contains greater GO content demonstrated greater photothermal conversion efficiency. Fig. 9 (c) shows that by manipulating the laser power, the temperature of profile of the selected sample (CS/RB-AgNPs/GO-1.5) can be fine-tuned. When 2 W power was used, the sample were heated to 45 °C within 100 s, which is within the therapeutic window for photothermal therapy applications. Fig. 9 (d) further illustrates the excellent photothermal conversion stability of the composite samples during cyclic heating/cooling tests.

4. Conclusions

In this study, we fabricated CS/RB-AgNPs/GO hybrid nanocomposite by incorporating GO into RT-APM synthesized CS/RB-AgNPs. The resulting nanocomposites have then been characterized towards several functional applications including multi-drug release, anti-microbial and photothermal conversion. The drug loading/release behaviour and the underlying mechanisms have been studied in detail using both single drug and dual drug models. Our composite system demonstrated pH sensitive release and the drug release profile can be best described by the Korsmeyer-Peppas model. The nanocomposite also demonstrated significant anti-microbial properties against E.coli an S.aureus bacteria strains as well as excellent photothermal conversion efficiency, which can be manipulated by tuning the laser power. These promising functionality may lead to the potential application of our nanocomposites in multiple fields, such as multi-therapeutic platform for the treatment of certain cancers, anti-microbial membranes/coatings, water treatment, etc.

Acknowledgments: The authors would like to acknowledge the financial support from China Scholarship Council (201806340039, 201606170059), China Postdoctoral Science Foundation (2020M671893), the Fundamental Research Funds for the Central Universities (WK9110000155), and

the Engineering and Physical Sciences Research Council (EPSRC) (EP/P00394X/1, EP/M015211/1 and EP/R008841/1).

Conflicts of Interest: Declare conflicts of interest or state "The authors declare no conflict of interest." Authors must identify and declare any personal circumstances or interest that may be perceived as inappropriately influencing the representation or interpretation of reported research results. Any role of the funders in the design of the study; in the collection, analyses or interpretation of data; in the writing of the manuscript, or in the decision to publish the results must be declared in this section. If there is no role, please state "The funders had no role in the design of the study; in the collection, analyses, or interpretation of data; in the writing of the manuscript, or in the decision to publish the results".

References

[1] Tao F, Cheng Y, Shi X, Zheng H, Du Y, Xiang W, et al. Applications of chitin and chitosan nanofibers in bone regenerative engineering. Carbohydrate Polymers. 2020;230:115658.

[2] Moeini A, Pedram P, Makvandi P, Malinconico M, Gomez d'Ayala G. Wound healing and antimicrobial effect of active secondary metabolites in chitosan-based wound dressings: A review. Carbohydrate Polymers. 2020;233:115839.

[3] Xu KL, Ganapathy K, Andl T, Wang Z, Copland JA, Chakrabarti R, et al. 3D porous chitosan-alginate scaffold stiffness promotes differential responses in prostate cancer cell lines. Biomaterials. 2019;217:12.

[4] Su Z, Wang H, Tian K, Xu F, Huang W, Tian X. Simultaneous reduction and surface functionalization of graphene oxide with wrinkled structure by diethylenetriamine (DETA) and their reinforcing effects in the flexible poly(2-ethylhexyl acrylate) (P2EHA) films. Composites Part A: Applied Science and Manufacturing. 2016;84:64-75.

[5] Park S, Ruoff RS. Chemical methods for the production of graphenes. Nat Nanotechnol. 2009;4(4):217-24.

[6] Shin SR, Li YC, Jang HL, Khoshakhlagh P, Akbari M, Nasajpour A, et al. Graphene-based materials for tissue engineering. Adv Drug Deliv Rev. 2016;105:255-74.

[7] Jiang Y, Yang Y, Zheng X, Yi Y, Chen X, Li Y, et al. Multifunctional load-bearing hybrid hydrogel with combined drug release and photothermal conversion functions. NPG Asia Materials. 2020;In press.

[8] Bai Y, Zhang J, Wen D, Gong P, Chen X. A poly (vinyl butyral)/graphene oxide composite with NIR light-induced shape memory effect and solid-state plasticity. Composites Science and Technology. 2019;170:101-8.

[9] Kalbacova M, Broz A, Kong J, Kalbac M. Graphene substrates promote adherence of human osteoblasts and mesenchymal stromal cells. Carbon. 2010;48(15):4323-9.

[10] Nayak TR, Andersen H, Makam VS, Khaw C, Bae S, Xu X, et al. Graphene for Controlled and Accelerated Osteogenic Differentiation of Human Mesenchymal Stem Cells. ACS Nano. 2011;5(6):4670-8.

[11] Barra A, Ferreira NM, Martins MA, Lazar O, Pantazi A, Jderu AA, et al. Eco-friendly preparation of electrically conductive chitosan - reduced graphene oxide flexible bionanocomposites for food packaging and biological applications. Composites Science and Technology. 2019;173:53-60.

[12] Hermenean A, Codreanu A, Herman H, Balta C, Rosu M, Mihali CV, et al. Chitosan-Graphene Oxide 3D scaffolds as Promising Tools for Bone Regeneration in Critical-Size Mouse Calvarial Defects. Sci Rep. 2017;7(1):16641.

[13] Rana VK, Choi M-C, Kong J-Y, Kim GY, Kim MJ, Kim S-H, et al. Synthesis and Drug-Delivery Behavior of Chitosan-Functionalized Graphene Oxide Hybrid Nanosheets. Macromolecular Materials and Engineering. 2011;296(2):131-40.

[14] Bao H, Pan Y, Ping Y, Sahoo NG, Wu T, Li L, et al. Chitosan-Functionalized Graphene Oxide as a Nanocarrier for Drug and Gene Delivery. Small. 2011;7(11):1569-78.

[15] Shamekhi MA, Mirzadeh H, Mahdavi H, Rabiee A, Mohebbi-Kalhori D, Baghaban Eslaminejad M. Graphene oxide containing chitosan scaffolds for cartilage tissue engineering. International Journal of Biological Macromolecules. 2019;127:396-405.

[16] Liu Y, Fang N, Liu B, Song L, Wen B, Yang D. Aligned porous chitosan/graphene oxide scaffold for bone tissue engineering. Materials Letters. 2018;233:78-81.

[17] Jiang L, Chen D, Wang Z, Zhang Z, Xia Y, Xue H, et al. Preparation of an Electrically Conductive Graphene Oxide/Chitosan Scaffold for Cardiac Tissue Engineering. Applied Biochemistry and Biotechnology. 2019;188(4):952-64.
[18] Saravanan S, Sareen N, Abu-El-Rub E, Ashour H, Sequiera GL, Ammar HI, et al. Graphene Oxide-Gold Nanosheets Containing Chitosan Scaffold Improves Ventricular Contractility and Function After Implantation into Infarcted Heart. Scientific Reports. 2018;8(1):15069.
[19] Karageorgiou V, Kaplan D. Porosity of 3D biomaterial scaffolds and osteogenesis. Biomaterials. 2005;26(27):5474-91.
[20] Hu X, Ren N, Chao Y, Lan H, Yan X, Sha Y, et al. Highly aligned graphene oxide/poly(vinyl alcohol) nanocomposite fibers with high-strength, antiultraviolet and antibacterial properties. Composites Part A: Applied Science and Manufacturing. 2017;102:297-304.
[21] Guo ZJ, Jiang N, Moore J, McCoy CP, Ziminska M, Rafferty C, et al. Nanoscale Hybrid Coating Enables Multifunctional Tissue Scaffold for Potential Multimodal Therapeutic Applications. Acs Applied Materials & Interfaces. 2019;11(30):27269-78.
[22] He M, Zhu C, Xu H, Sun D, Chen C, Feng G, et al. Conducting Polyetheretherketone Nanocomposites with an Electrophoretically Deposited Bioactive Coating for Bone Tissue Regeneration and Multimodal Therapeutic Applications. ACS Applied Materials & Interfaces. 2020;12(51):56924-34.
[23] Jiang Y, Yang Y, Zheng X, Yi Y, Chen X, Li Y, et al. Multifunctional load-bearing hybrid hydrogel with combined drug release and photothermal conversion functions. NPG Asia Materials. 2020;12(1):18.
[24] Sun D, Turner J, Jiang N, Zhu S, Zhang L, Falzon BG, et al. Atmospheric pressure microplasma for antibacterial silver nanoparticle/chitosan nanocomposites with tailored properties. Composites Science and Technology. 2020;186:107911.
[25] Marcano DC, Kosynkin DV, Berlin JM, Sinitskii A, Sun Z, Slesarev A, et al. Improved Synthesis of Graphene Oxide. ACS Nano. 2010;4(8):4806-14.
[26] Su Z, Wang H, Tian K, Huang W, Guo Y, He J, et al. Multifunctional anisotropic flexible cycloaliphatic epoxy resin nanocomposites reinforced by aligned graphite flake with non-covalent biomimetic functionalization. Composites Part A: Applied Science and Manufacturing. 2018;109:472-80.
[27] Suyatma NE, Tighzert L, Copinet A, Coma V. Effects of Hydrophilic Plasticizers on Mechanical, Thermal, and Surface Properties of Chitosan Films. Journal of Agricultural and Food Chemistry. 2005;53(10):3950-7.
[28] Leszczynska A, Pielichowski K. Application of thermal analysis methods for characterization of polymer/montmorillonite nanocomposites. Journal of Thermal Analysis and Calorimetry. 2008;93(3):677-87.
[29] Zou J, Kim F. Self-Assembly of Two-Dimensional Nanosheets Induced by Interfacial Polyionic Complexation. ACS Nano. 2012;6(12):10606-13.
[30] Yao Z, Braidy N, Botton GA, Adronov A. Polymerization from the Surface of Single-Walled Carbon Nanotubes − Preparation and Characterization of Nanocomposites. Journal of the American Chemical Society. 2003;125(51):16015-24.
[31] González-Campos JB, Mota-Morales JD, Kumar S, Zárate-Triviño D, Hernández-Iturriaga M, Prokhorov Y, et al. New insights into the bactericidal activity of chitosan-Ag bionanocomposite: The role of the electrical conductivity. Colloids and Surfaces B: Biointerfaces. 2013;111:741-6.
[32] Xu K, Liu C, Kang K, Zheng Z, Wang S, Tang Z, et al. Isolation of nanocrystalline cellulose from rice straw and preparation of its biocomposites with chitosan: Physicochemical characterization and evaluation of interfacial compatibility. Composites Science and Technology. 2018;154:8-17.
[33] Jin L, Bai R. Mechanisms of Lead Adsorption on Chitosan/PVA Hydrogel Beads. Langmuir. 2002;18(25):9765-70.
[34] Hasan A, Waibhaw G, Saxena V, Pandey LM. Nano-biocomposite scaffolds of chitosan, carboxymethyl cellulose and silver nanoparticle modified cellulose nanowhiskers for bone tissue engineering applications. International Journal of Biological Macromolecules. 2018;111:923-34.

[35] Khawaja H, Zahir E, Asghar MA, Asghar MA. Graphene oxide, chitosan and silver nanocomposite as a highly effective antibacterial agent against pathogenic strains. Colloids and Surfaces A: Physicochemical and Engineering Aspects. 2018;555:246-55.
[36] Kim Y-H, Tabata Y. Dual-controlled release system of drugs for bone regeneration. Advanced Drug Delivery Reviews. 2015;94:28-40.
[37] 5 - Mathematical models of drug release. In: Bruschi ML, editor. Strategies to Modify the Drug Release from Pharmaceutical Systems: Woodhead Publishing; 2015. p. 63-86.
[38] Korsmeyer RW, Gurny R, Doelker E, Buri P, Peppas NA. Mechanisms of solute release from porous hydrophilic polymers. International Journal of Pharmaceutics. 1983;15(1):25-35.
[39] Peppas NA, Korsmeyer R. Dynamically swelling hydrogels in controlled release applications. Hydrogels in medicine and pharmacy. 1987;3:109-36.
[40] Saurí J, Millán D, Suñé-Negre JM, Colom H, Ticó JR, Miñarro M, et al. Quality by Design approach to understand the physicochemical phenomena involved in controlled release of captopril SR matrix tablets. International Journal of Pharmaceutics. 2014;477(1):431-41.
[41] Kevadiya BD, Chettiar SS, Rajkumar S, Bajaj HC, Brahmbhatt H, Chaudhari JC, et al. Evaluation of Montmorillonite/Poly (L-Lactide) microcomposite spheres as ambidextrous reservoirs for controlled release of Capecitabine (Xeloda) and assessment of cell cytotoxic and oxidative stress markers. Composites Science and Technology. 2014;90:193-201.
[42] Higuchi T. Rate of Release of Medicaments from Ointment Bases Containing Drugs in Suspension. Journal of Pharmaceutical Sciences. 1961;50(10):874-5.
[43] Casalini T, Salvalaglio M, Perale G, Masi M, Cavallotti C. Diffusion and Aggregation of Sodium Fluorescein in Aqueous Solutions. The Journal of Physical Chemistry B. 2011;115(44):12896-904.
[44] Xing K, Fan R, Wang F, Nie H, Du X, Gai S, et al. Dual-Stimulus-Triggered Programmable Drug Release and Luminescent Ratiometric pH Sensing from Chemically Stable Biocompatible Zinc Metal–Organic Framework. ACS Applied Materials & Interfaces. 2018;10(26):22746-56.
[45] Le Pape H, Solano-Serena F, Contini P, Devillers C, Maftah A, Leprat P. Involvement of reactive oxygen species in the bactericidal activity of activated carbon fibre supporting silver: Bactericidal activity of ACF(Ag) mediated by ROS. Journal of Inorganic Biochemistry. 2004;98(6):1054-60.
[46] Qiu J, Geng H, Wang D, Qian S, Zhu H, Qiao Y, et al. Layer-Number Dependent Antibacterial and Osteogenic Behaviors of Graphene Oxide Electrophoretic Deposited on Titanium. ACS Applied Materials & Interfaces. 2017;9(14):12253-63.
[47] Ma J, Zhang J, Xiong Z, Yong Y, Zhao XS. Preparation, characterization and antibacterial properties of silver-modified graphene oxide. Journal of Materials Chemistry. 2011;21(10):3350-2.

Figure captions:

Preprints (www.preprints.org) | NOT PEER-REVIEWED | Posted: 12 April 2021 doi:10.20944/preprints202104.0311.v1

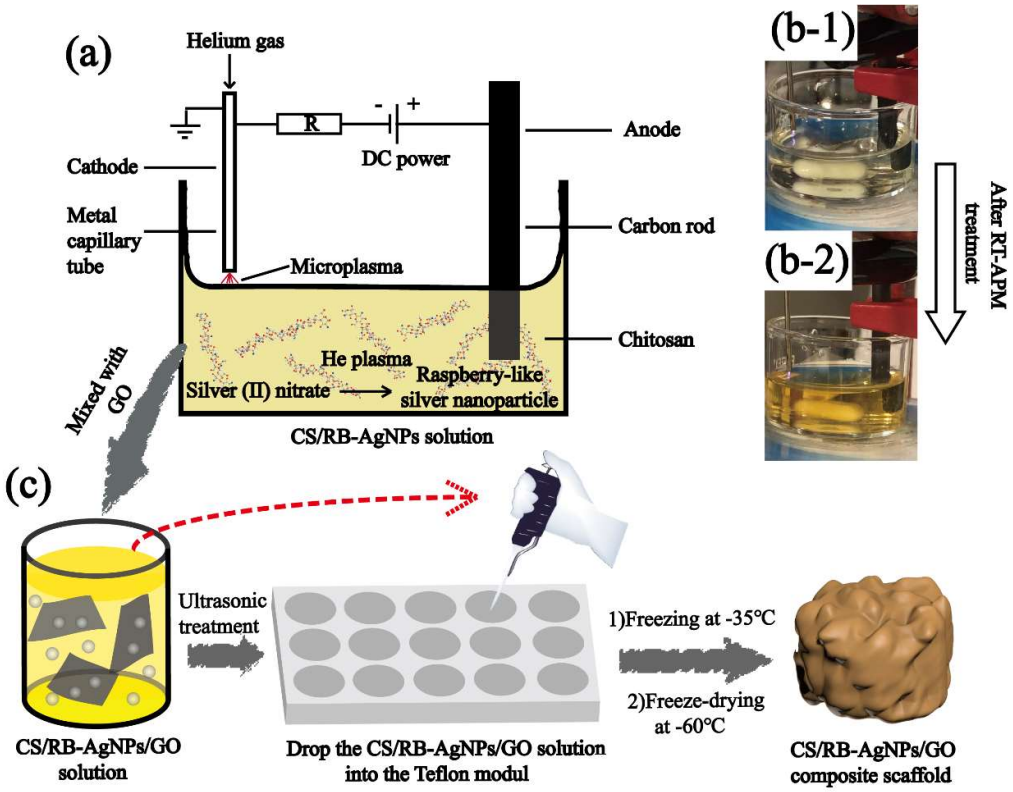

Scheme 1. (a) The schematic diagram of the atmospheric pressure microplasma setup for the preparation of CS/RB-AgNPs solutions; (b) CS+AgNO3 solution before and after RT-APM treatment and (c) the preparation of CS/RB-AgNPs/GO nanocomposite by freeze-drying process (For interpretation of the references to color in this figure legend, the reader is referred to the web version of this article.).

Preprints (www.preprints.org) | NOT PEER-REVIEWED | Posted: 12 April 2021 doi:10.20944/preprints202104.0311.v1

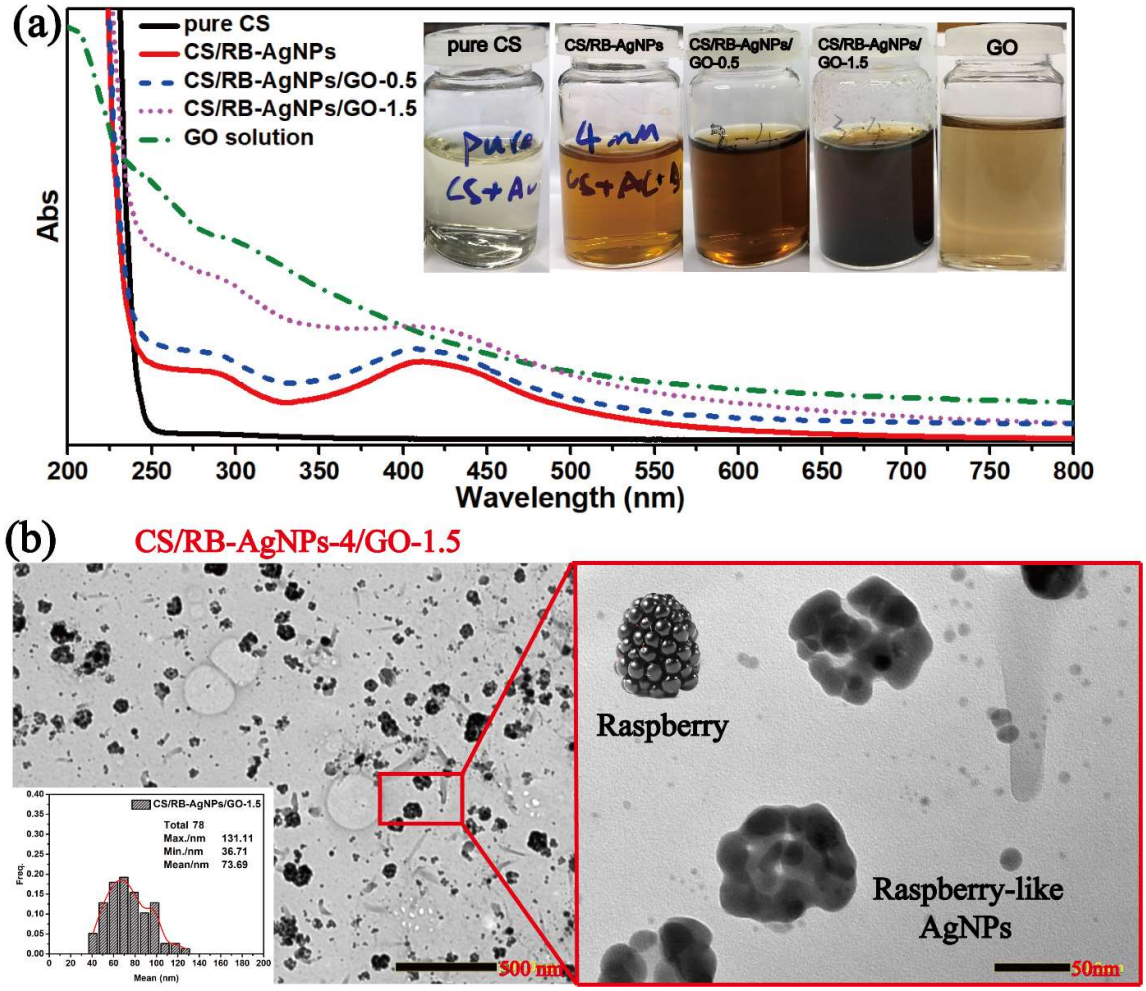

Figure 1. (a) UV-vis spectra of all sample solutions and (b) TEM image of the RB-AgNPs with size distribution (For interpretation of the references to color in this figure legend, the reader is referred to the web version of this article.).

Preprints (www.preprints.org) | NOT PEER-REVIEWED | Posted: 12 April 2021 doi:10.20944/preprints202104.0311.v1

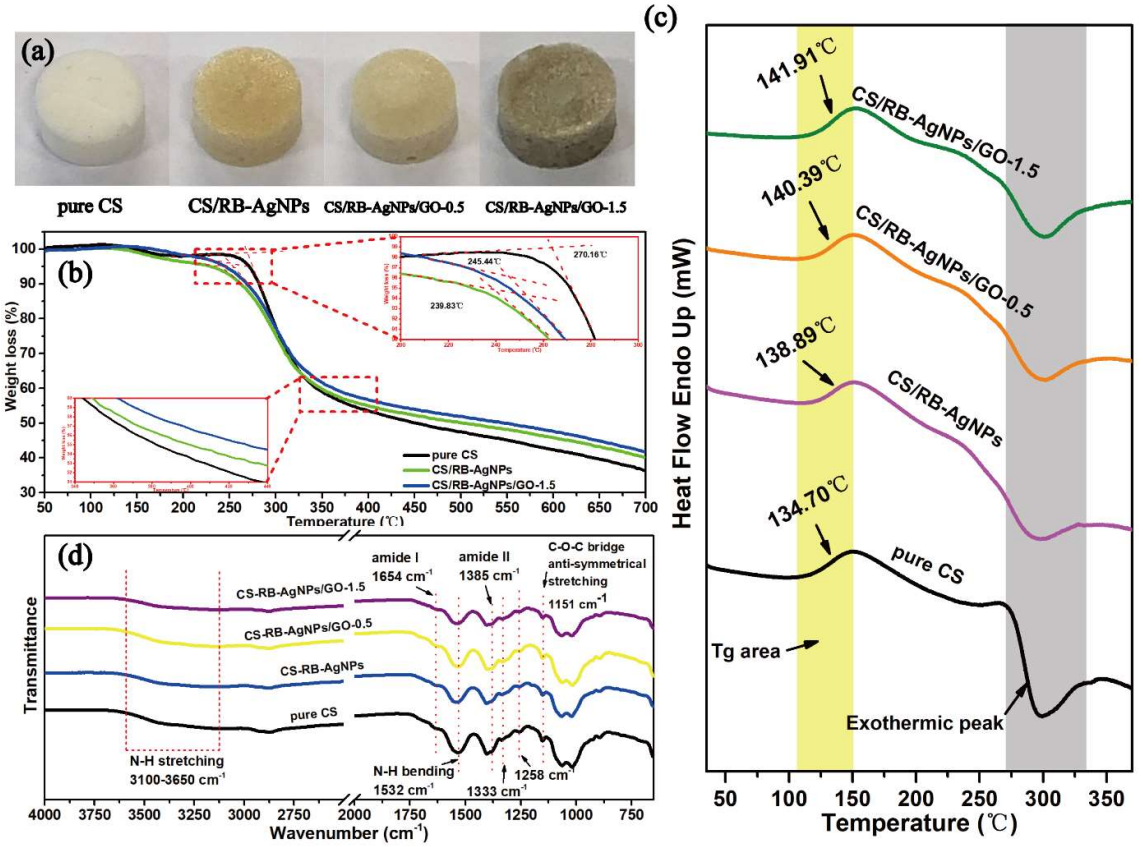

Figure 2. (a) The photographs of typical nanocomposite samples; (b) TGA curve, (c) DSC curve obtained from the second heating, and (d) The FT-IR spectra of pure CS, CS/RB-AgNPs, and CS/RB-AgNPs/GO nanocomposites (For interpretation of the references to color in this figure legend, the reader is referred to the web version of this article.).

Preprints (www.preprints.org) | NOT PEER-REVIEWED | Posted: 12 April 2021 doi:10.20944/preprints202104.0311.v1

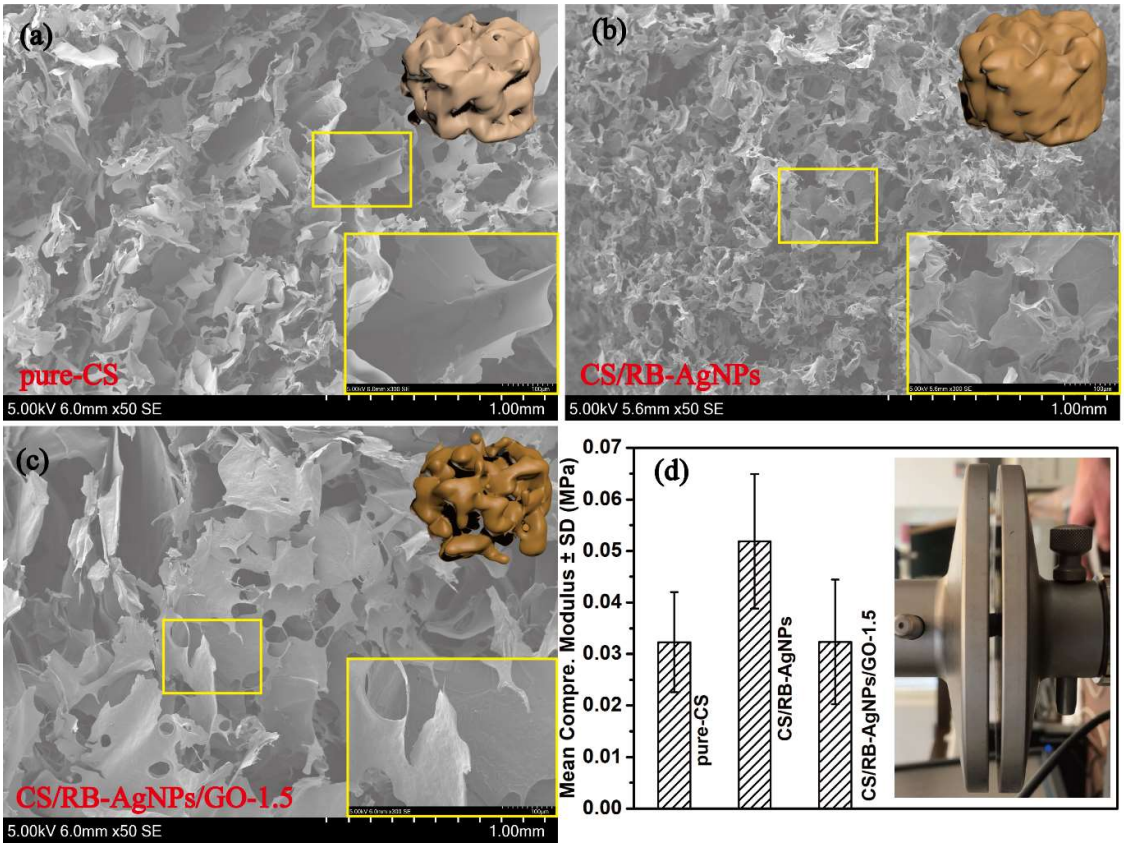

Figure 3. SEM images of (a) pure CS, (b) CS/RB-AgNPs, (c) CS/RB-AgNPs/GO-0.5, and (d) mean compressive elastic modulus of nanocomposite samples (n=3 for each group) (For interpretation of the references to color in this figure legend, the reader is referred to the web version of this article.).

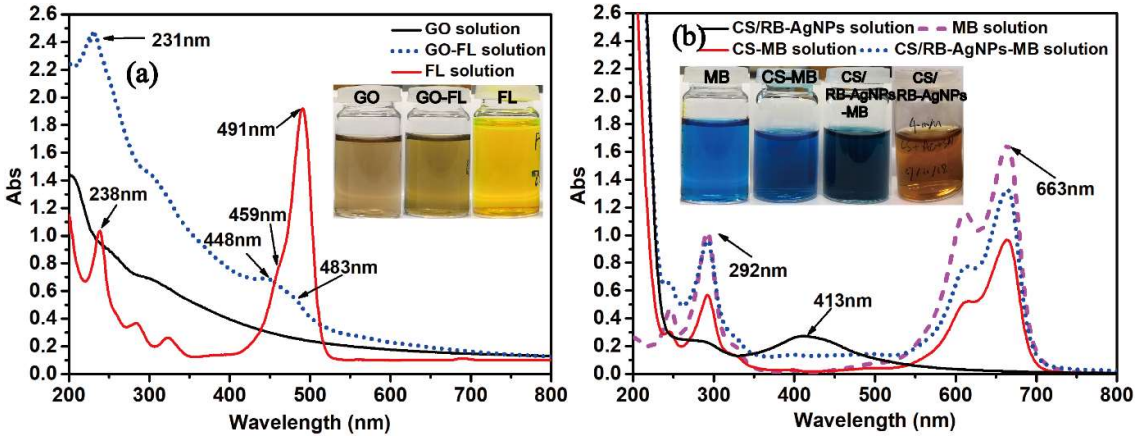

Figure 4. (a) UV-vis spectra of GO, GO-FL, FL solutions and (b) MB, CS/RB-AgNPs-MB, CS-MB, and CS/RB-AgNPs solutions; Inset: photos showing colours of each as-prepared solution (For interpretation of the references to color in this figure legend, the reader is referred to the web version of this article.).

Preprints (www.preprints.org) | NOT PEER-REVIEWED | Posted: 12 April 2021 doi:10.20944/preprints202104.0311.v1

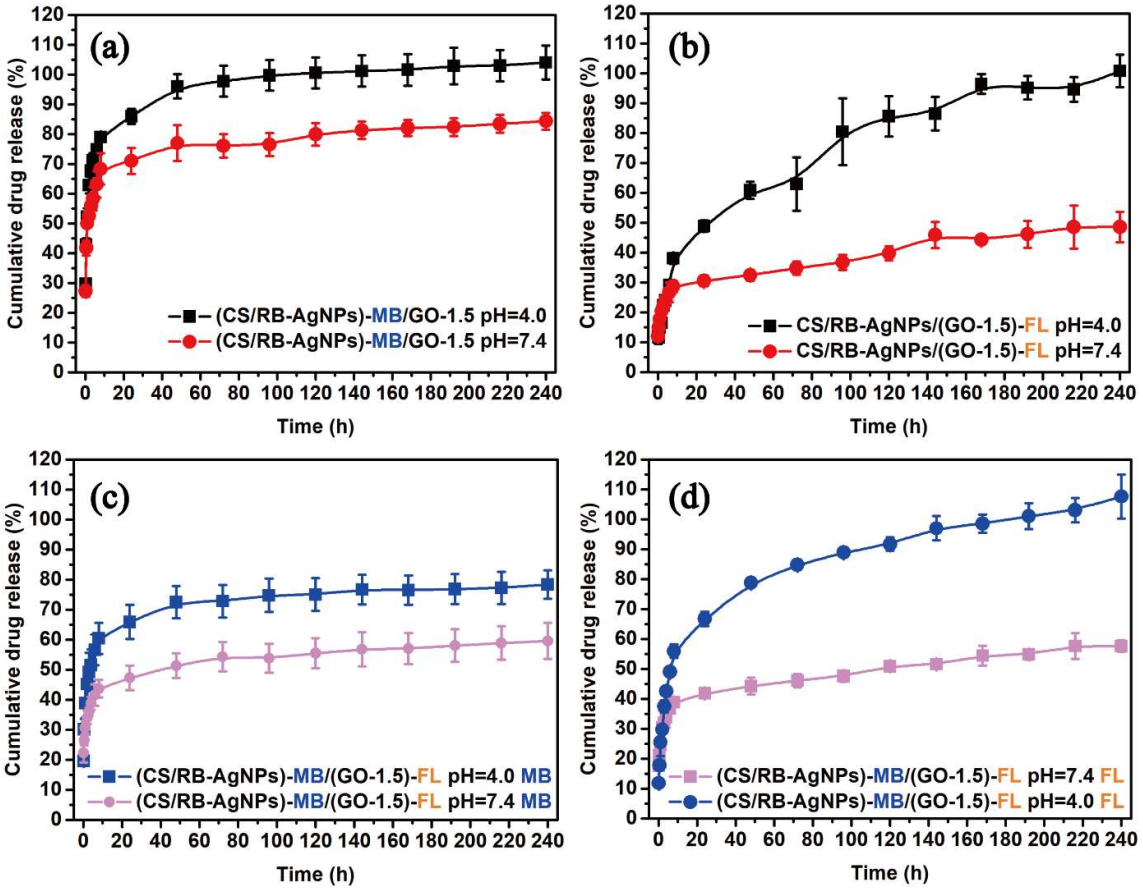

Figure 5. (a) Single drug release profile of MB; (b) single drug release profile of FL; and dual drug release profile of (c) MB and (d) FL from CS/RB-AgNPs/GO-1.5 (For interpretation of the references to color in this figure legend, the reader is referred to the web version of this article.).

Preprints (www.preprints.org) | NOT PEER-REVIEWED | Posted: 12 April 2021 doi:10.20944/preprints202104.0311.v1

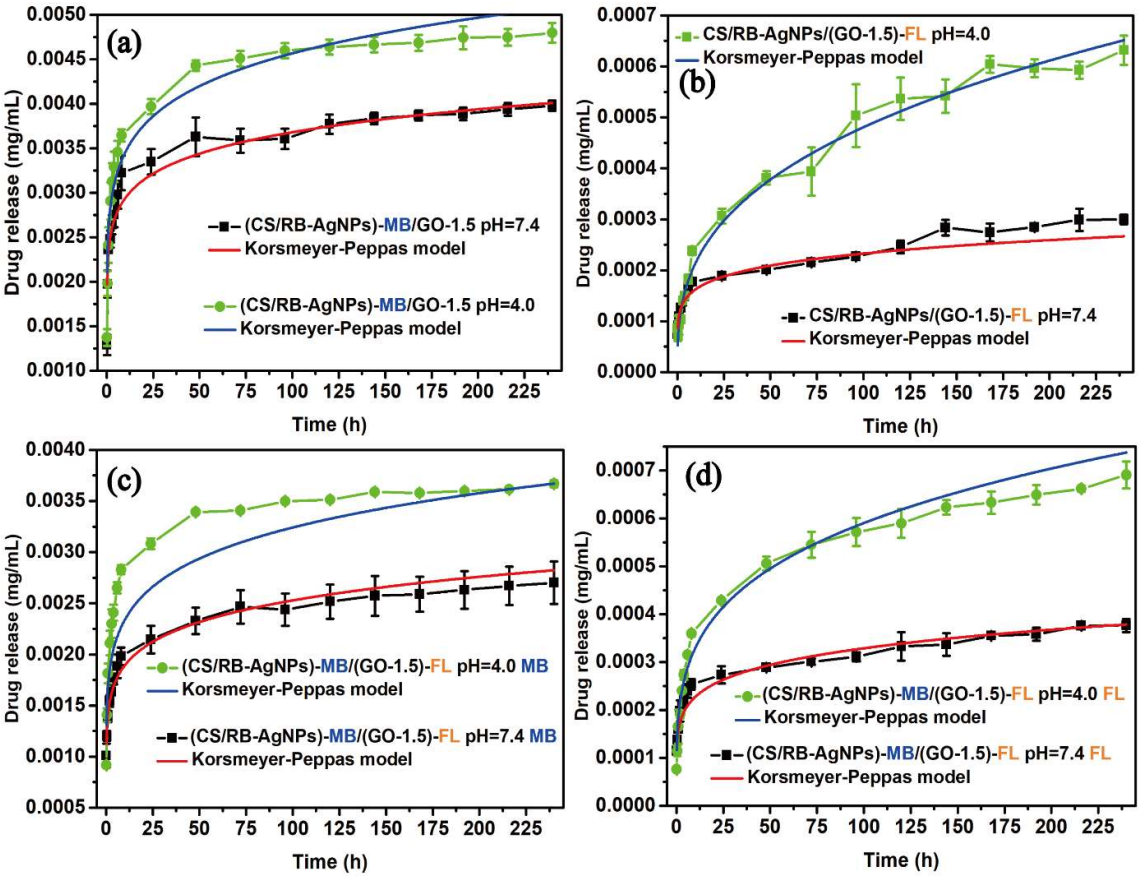

Figure 6. Fitting of single and dual drug release curves to Korsmeyer-Peppas model (solid lines) (For interpretation of the references to color in this figure legend, the reader is referred to the web version of this article.).

Preprints (www.preprints.org) | NOT PEER-REVIEWED | Posted: 12 April 2021 doi:10.20944/preprints202104.0311.v1

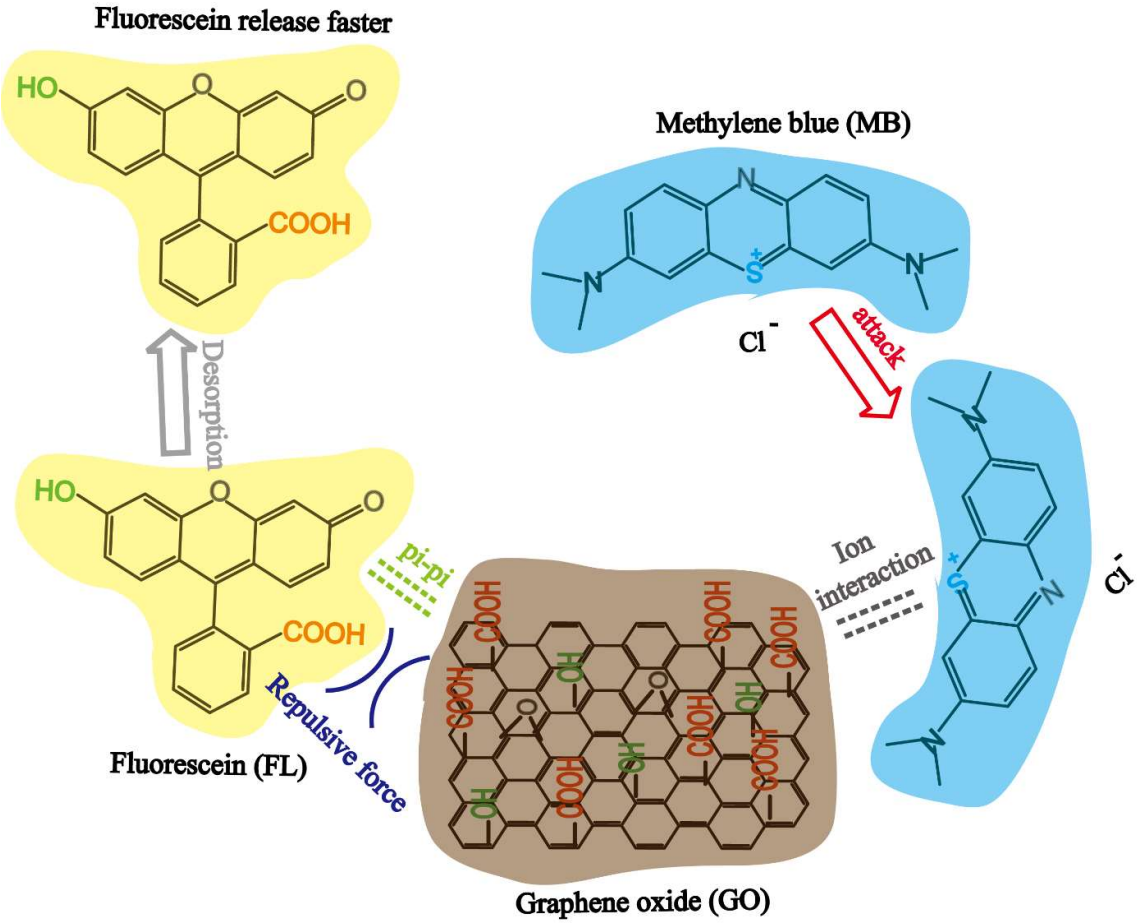

Figure 7. The interaction mechanism of GO, MB and FL (For interpretation of the references to color in this figure legend, the reader is referred to the web version of this article.).

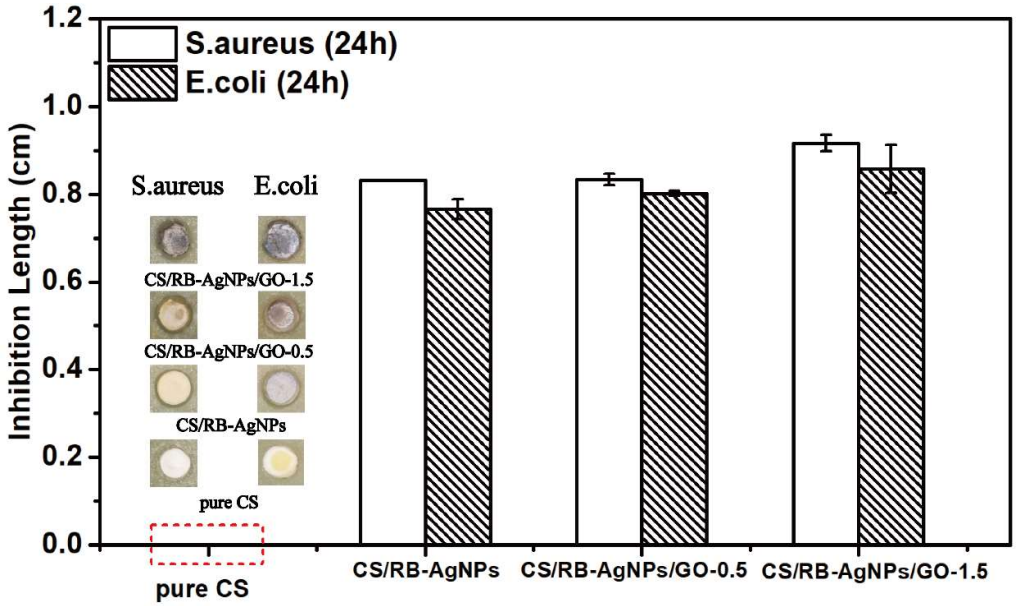

Figure 8. Antibacterial behaviour of nanocomposite samples against *S. aureus* and *E. coli* (For interpretation of the references to color in this figure legend, the reader is referred to the web version of this article.).

Preprints (www.preprints.org) | NOT PEER-REVIEWED | Posted: 12 April 2021 doi:10.20944/preprints202104.0311.v1

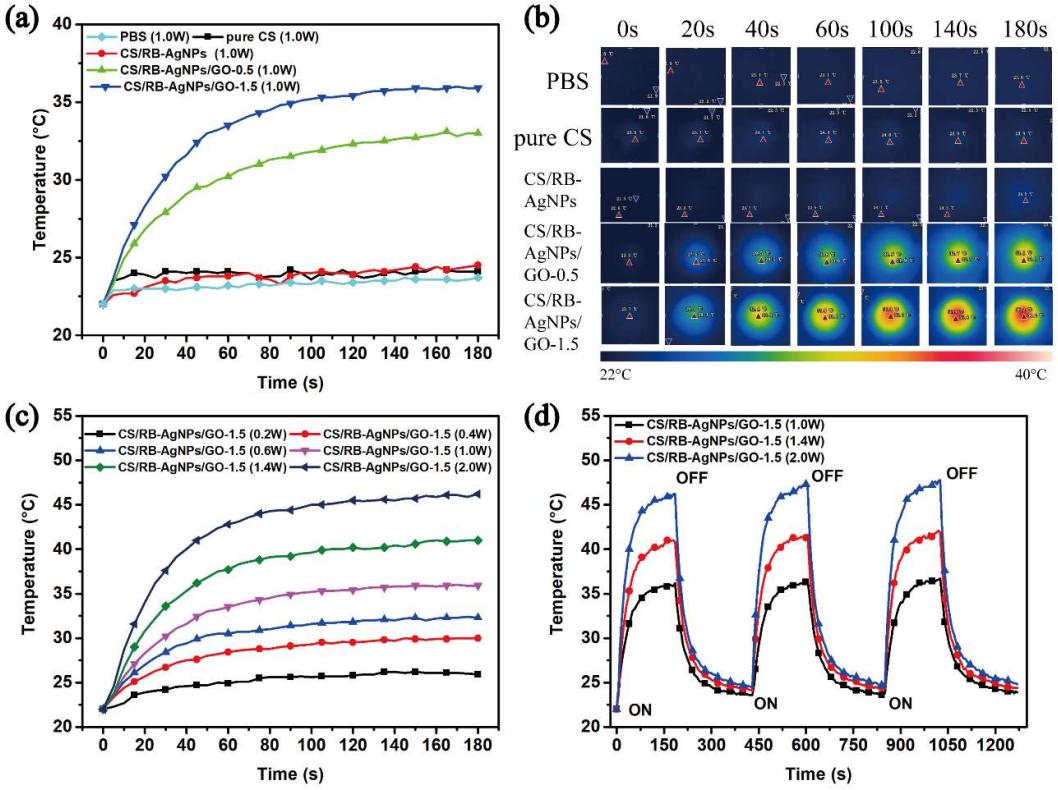

Figure 9. Photothermal conversion of all testing samples (a) Temperature profile and (b) IR thermal images of PBS solution control, pure CS, CS/RB-AgNPs, CS/RB-AgNPs/GO-0.5, and CS/RB-AgNPs/GO-1.5 under 808 nm continuous wavelength laser irradiation (1.0 W) from 0 to 3 min. (c) Temperature profile of CS/RB-AgNPs/GO-1.5 with different power from 0.2 to 2.0 W. (d) Photothermal conversion stability of CS/RB-AgNPs/GO-1.5 irradiated by 808 nm laser (power: 1.0, 1.4, and 2.0 W). The sample was irradiated by 3 min and then cooled down to 23 °C with three repeating cycles (For interpretation of the references to color in this figure legend, the reader is referred to the web version of this article.).

Tables:

Table 1 Nomenclatures of Samples and Their Preparation Methods.

Preprints (www.preprints.org) | NOT PEER-REVIEWED | Posted: 12 April 2021 doi:10.20944/preprints202104.0311.v1

Sample name	GO wt % (vs CS)	$AgNO_3$ / CS precursor concentration	RT-APM
Pure CS	none	none	no
CS/RB-AgNPs	none	4.0 mM $AgNO_3$	yes
CS/RB-AgNPs/GO-0.5	0.5 % (w/w)	4.0 mM $AgNO_3$	yes
CS/RB-AgNPs/GO-1.5	1.5 % (w/w)	4.0 mM $AgNO_3$	yes

Table 2. The kinetic parameters in Korsmeyer-Peppas models.

Sample code	Korsmeyer-Peppas model fit all range		
	D_K ($\times 10^{-5}$ cm^2s^{-1})	N	R^2
(CS/RB-AgNPs)-MB/GO-1.5 pH=7.4	1.573	0.098	0.983
(CS/RB-AgNPs)-MB/GO-1.5 pH=4.0	1.949	0.121	0.915
CS/RB-AgNPs/(GO-1.5)-FL pH=7.4	0.0231	0.155	0.981
CS/RB-AgNPs/(GO-1.5)-FL pH=4.0	0.0168	0.347	0.986
(CS/RB-AgNPs)-MB/(GO-1.5)-FL pH=7.4 MB	0.572	0.126	0.969
(CS/RB-AgNPs)-MB/(GO-1.5)-FL pH=4.0 MB	0.811	0.142	0.936
(CS/RB-AgNPs)-MB/(GO-1.5)-FL pH=7.4 FL	0.0437	0.161	0.995
(CS/RB-AgNPs)-MB/(GO-1.5)-FL pH=4.0 FL	0.0596	0.254	0.968